

Interface engineering of organic-inorganic heterojunctions with enhanced charge transfer



Yizhou Wu^{b,e,1}, Yu Chen^{a,1}, Donglin Li^b, Dania Sajjad^g, Yixuan Chen^b, Yiying Sun^b, Shusong Liu^a, Jiafu Shi^{a,c,d,*}, Zhongyi Jiang^{b,d,f,**}

^a School of Environmental Science and Engineering, Tianjin University, 92# Weijin Road, Nankai District, Tianjin 300072, China

^b Key Laboratory for Green Chemical Technology of Ministry of Education, School of Chemical Engineering and Technology, Tianjin University, 92# Weijin Road, Nankai District, Tianjin 300072, China

^c State Key Laboratory of Biochemical Engineering, Institute of Process Engineering, Chinese Academy of Sciences, Beijing 100190, China

^d Collaborative Innovation Center of Chemical Science and Engineering (Tianjin), Tianjin 300072, China

^e Center of Artificial Photosynthesis for Solar Fuels, School of Science, Westlake University, Hangzhou 310024, China

^f Joint School of National University of Singapore and Tianjin University, International Campus of Tianjin University, Binhai New City, Fuzhou 350207, China

^g Department of Chemical and Biological Engineering, University of Ottawa, 161 Louis Pasteur Private, Ottawa, Ontario K1N 6N5, Canada

ARTICLE INFO

Keywords:

Interface
Charge transfer
Heterojunction
Photocatalysis
Nicotinamide regeneration

ABSTRACT

Heterostructure materials are increasingly utilized in solar energy conversion to pursue high efficiency and long-term stability. The charge transfer across interfaces gives rise to major energy loss arising from non-ideal interfacial effects, i.e., high interfacial energy barrier and low interfacial contacting area. Herein, we demonstrate a facile interface engineering strategy to eliminate non-ideal interfacial effects. A heterojunction of CN@C-P25 is constructed via polyphenol-assisted assembly of titania (P25) and carbon nitride (CN). The uniform dispersion of P25 on CN enlarges the interfacial contacting area of 3.2-fold compared with random dispersion, while the transformation of polyphenols into conjugated carbon facilitates the interfacial charge transfer by switching a 0.4 eV Schottky contact to a 0.1 eV Ohmic contact between CN and P25. A 2.5-fold enhancement of charge transfer flux is obtained with an initial reaction rate of $5185 \mu\text{mol h}^{-1} \text{g}^{-1}$ for photocatalytic nicotinamide regeneration.

1. Introduction

Conversion and utilization of solar energy in artificial approaches more efficiently and flexibly than the natural archetype is one of the “Holy Grail” research in chemistry [1–5]. Solar energy in photons is firstly converted to active chemical energy in charge carriers by light absorbents. The charge carriers are utilized through different approaches to produce electricity or chemicals, including solar cells [6,7], photoelectrochemistry [8,9], photocatalysis [10,11], etc. To pursue high-efficiency and long-term stability, composite materials with heterostructures such as sandwich structure [12], mixed-dimensional structure [13], and core-shell structure [14] are highly preferred, where interfaces are generated inevitably. To fulfill the energy

conversion, the excited charge carriers are required to transfer from the birth site to either electrode or reaction site through the interfaces. Energy loss during the interfacial charge transfer constitutes one of the primary energy consumptions in these applications, also in relevant fields such as light emitting diode and electrocatalysis [15,16]. In general, the inefficient charge transfer is primarily impeded by non-ideal interfacial effects, i.e., over high interfacial energy barrier and low interfacial contacting area, both of which lead to the accumulation of charge carriers at the interface. Despite the self-consumed energy loss of the interfacial charges in forms of heat or self-luminous, the charge accumulation may also cause structural damage at the interface, leading to irreversible drop of the charge transfer efficiency and exacerbating the energy loss. Strategies to suppress the non-ideal interfacial effects

* Corresponding author at: School of Environmental Science and Engineering, Tianjin University, 92# Weijin Road, Nankai District, Tianjin 300072, China.

** Corresponding author at: Key Laboratory for Green Chemical Technology of Ministry of Education, School of Chemical Engineering and Technology, Tianjin University, 92# Weijin Road, Nankai District, Tianjin 300072, China.

E-mail addresses: shijiafu@tju.edu.cn (J. Shi), zhyjiang@tju.edu.cn (Z. Jiang).

¹ The authors contributed equally.

are in great demand to pursue high efficiency of solar energy conversion.

In theory, the interfacial energy barrier is primarily arisen from the mismatching energy level (molecular orbital or band position) of two neighboring materials, which tends to form Schottky contact and hinders the charge transfer by the reversed electric field [17]. Doping/defect engineering is commonly used to reduce the energy barrier [18]. The energy level could be shifted to favorable direction through the hybridization between subject and dopant/defect [19]. Doping of oxygen in the triazine of g-C₃N₄ provides a mid-gap state near the conduction band, offering higher electron density favorable for photocatalytic reduction [20]. The dopant/defect may also introduce an impurity energy level to facilitate the charge transfer. Nitrogen-defective g-C₃N₄ exhibits an 18-fold higher activity compared with pristine g-C₃N₄ due to the improved light harvesting by the narrowed band gap as well as the inhibited charge recombination by the spatial separation of HOMOs and LUMOs [21]. Introducing an interlayer with an in-between energy level is an alternative way to re-arrange the energy level between two materials, which may switch the Schottky contact to an Ohmic contact. The utilization of gold or carbon layer in photocatalyst sheets could promote the charge transfer between oxygen evolution catalysts and hydrogen evolution catalysts, leading to a solar-to-hydrogen efficiency up to 1.2% [11,22]. The adjustment of energy level could enhance the charge transfer by 2–10 folds [23–25]. Furthermore, developing intermolecular conjugation of electron cloud, such as π - π stacking, would also facilitate the interfacial charge transfer at molecular level [26]. Construction of g-C₃N₄/PDI-g-C₃N₄ heterojunction efficiently facilitates the charge separation at different domains, leading to an 8-fold enhancement of the activity for H₂O₂ generation [27]. The π - π interaction between Ti₃C₂ and PDIsm not only leads to an easy self-assembly during material preparation but also promotes the charge separation and migration during photocatalysis [28].

Even that a favorable energy barrier could enhance the charge transfer, the overall charge transfer efficiency would still be limited by the low interfacial contacting area between two neighboring materials. In this regard, various heterostructures have been exploited to enlarge the interfacial contacting area, such as two-dimensional laminate structure [29], mixed-dimensional structure [30], core-shell/multi-shell structure [31,32], etc. Zero-dimensional Cu-Fe bi-metal oxide is loaded on 2D g-C₃N₄ to construct a heterostructure photocatalyst. The synergy of Cu-Fe site promotes the charge extraction from g-C₃N₄ and benefits the H₂O₂ absorption/activation, leading to efficient photocatalysis-Fenton oxidation [33]. Hierarchical PPY@ZnIn₂S₄ nanocomposite is fabricated through in-situ growth of 2D ZnIn₂S₄ nanosheets on 1D polypyrrole nanotubes. PPY nanotubes act as an electron collector to promote the charge separation, leading to a remarkable utilization of charge carriers in simultaneous H₂ evolution and 1,4-benzenedimethanol oxidation [34]. A core-shell Au@NiS_{1+x} modified TiO₂ ternary heterojunction photocatalyst is designed for H₂ evolution. The surface loaded Au nanoparticles extract the photo-generated electrons from TiO₂ and subsequently transfer these electrons to the S-enriched shell of NiS_{1+x}. The rapid generation of electron-enriched S ^{$\delta-$} active sites lowers the hydrogen absorption on S atom, facilitating the formation of H₂ molecule [35]. Nano-porous structure or framework structure has also been utilized for the interface construction due to their unparalleled functions in expanding the interface to nanoscale or molecular scale, respectively [36,37]. Metal-organic frameworks of UiO-bpydc are modified by Zn for photocatalytic CO₂ cycloaddition. Zn acts as an additional electron acceptor at the ligand/metal interface to promote the ligand-to-metal charge transfer and ultimately benefits to CO₂ activation [38]. Covalent heptazine frameworks consisted of heptazine moiety and acetylene/diacetylene moiety are applied for H₂O₂ generation. The charge separation at the interface of the two moieties results in a spatial separation of two-electron oxygen reduction and two-electron water oxidation, achieving a solar-to-chemical efficiency of 0.78% [39]. Despite the

efforts in lowering the interfacial energy barrier or enlarging the interfacial contacting area, intensifying the interfacial charge transfer remains one of the grand challenges. Therefore, alternative strategies are highly desired to simultaneously lower the energy barrier and enlarge the interfacial contacting area.

To demonstrate the concept, in our study, one organic semiconductor of graphitic carbon nitride (CN) and one inorganic semiconductor of titania (the commercial nanoparticles, P25) are screened to construct the heterojunction photocatalysts. The controllable construction of the organic-inorganic interface by two typical semiconductors may inspire the design of charge transfer interfaces in photocatalysis and other applications. By taking advantages of the metal coordination ability and the surface coating property of polyphenols, we prepared a carbon-mediated organic-inorganic heterojunction photocatalyst, CN@C-P25, through the calcination of one-step assembled melamine@polyphenol-P25 precursor (**Scheme 1**). The polyphenol (tannic acid, TA) was coordinated with P25 and then non-selectively coated on the surface of melamine, leading to a uniform dispersion of P25 on CN after calcination, which remarkably increased the interfacial contacting area. Meanwhile, the energy barrier between P25 and CN was reduced by TA-transformed C moiety. The incorporation of C moiety created an intermediate energy level, which intensified the electron injection from CN to P25 via π - π stacking between conjugated C moiety and tri-s-triazine. Accordingly, a 0.4 eV Schottky contact between CN and P25 was switched to a 0.1 eV Ohmic contact using C moiety as the interlayer, while the relative interfacial contacting area was increased by 3.2 folds compared with the randomly distributed P25 on CN. CN@C-P25 exhibited a 2.5-fold enhancement of charge transfer flux due to the well-suppressed non-ideal interfacial effects. When applied for photocatalytic regeneration of reduced form of nicotinamide-adenine dinucleotide (NADH, a commonly used cofactor in oxidoreductase-catalyzed reactions [40–42]), a yield of 77.3% with an initial reaction rate of 5185 $\mu\text{mol h}^{-1} \text{g}^{-1}$ were obtained. A greener route for NADH regeneration was also demonstrated by substituting the conventional sacrificial electron donor of triethanolamine with biomass, and a moderate NADH yield of 33.7% was obtained.

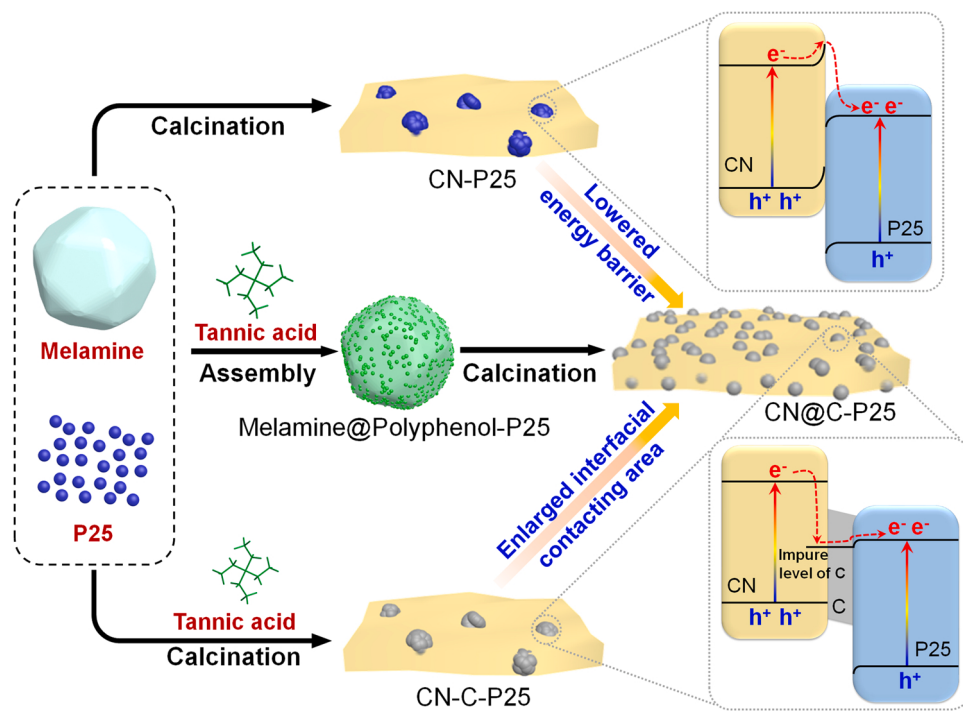
2. Experimental section

2.1. Materials

Melamine (99%), triethanolamine (TEOA, \geq 99% GC), disodium hydrogen phosphate (AR, 99%), sodium dihydrogen phosphate (AR), and tannic acid (ACS) were obtained from J&K Chemical, Beijing. Formaldehyde (stabilized with 10–15% methanol), alcohol dehydrogenase (powder, 321 units/mg protein), β -nicotinamide adenine dinucleotide hydrate (\geq 98%) and D-(+)-glucose were received from Sigma-Aldrich, Shanghai. Titanium (IV) oxide and hydrochloric acid (HCl, 36.0–38.0 wt%) were obtained from Rionion, Tianjin. Acetonitrile (GR) was obtained from Concord Technology, Tianjin. Phosphoric acid (95%) and D-(+)-xylose were purchased from Aladdin, Shanghai. Sodium hydroxide (AR) was received from Kermel, Tianjin. Propyl aldehyde (98%) was obtained from TCI, Shanghai.

2.2. Synthesis of CN@C-P25 photocatalysts

In general, 1 g of melamine and 100 mg of P25 were added into a 25 mL breaker. 10 mL deionized (DI) water was then dropped into the breaker. The resultant solution was ultrasonicated for 20 min. After that, 50 mg of tannic acid solution (10 mg mL⁻¹) was put into the solution under vigorous stirring. It can be observed that the color of solution changed from white to orange instantly. The modification process was kept stirring for 5 min. The product, named as melamine@polyphenol-P25, was purified through centrifugation using DI water and then freeze-dried for 12 h. After being ground into powders, melamine@polyphenol-P25 was transferred into a crucible which was



Scheme 1. Design of interface-engineered organic-inorganic heterojunctions with lowered energy barrier and enlarged interfacial contacting area.

sealed with tin foil paper. The crucible was then calcinated in a muffle furnace with the following procedure: 300 °C for 1 h, 400 °C for 1 h, and 550 °C for 4 h. After calcination, the as obtained CN@C-P25 photocatalysts were ground into powders for further use. To prepare CN@C-P25-X, melamine@polyphenol-P25-X was obtained by adding X mg of TA ($X = 10, 50, 100, 200$) to the solution, which was then collected, freeze-dried and calcined with the same procedure as mentioned above. To prepare CN-P25, 1 g of melamine and 100 mg of P25 were mixed in a mortar until formed homogeneous powders. Then, the mixture powders were calcinated with the same procedure of CN@C-P25. As for CN-C-P25, 1 g of melamine, 100 mg of P25 and 50 mg of TA were grounded into well-mixed powders and then calcined with the same procedure. The yield of these photocatalyst samples was about 400–500 mg.

2.3. Procedure of photocatalytic NADH regeneration

Photocatalytic NADH regeneration was performed in a 3.1 mL quartz cuvette ($10 \times 10 \times 31$ mm, with an unsealed PTFE cover) with a total reaction volume of 2 mL and a pH value of 8.0 (Notably, a higher activity of photocatalytic NADH regeneration could be obtained with increased pH value in the range of 6.0–9.0. Considering the activity of NADH regeneration and enzymes, the regular pH value was chosen as 8.0). The reaction solution contained phosphate buffered solution (PBS, 100 mmol mL^{-1}), TEOA ($1000 \text{ mmol mL}^{-1}$), well-dispersed photocatalyst (1 mg mL^{-1}), co-catalyst of Rh (0.2 mmol mL^{-1}) and NAD⁺ (1 mmol mL^{-1}). In addition, CN and P25 were chosen for the control group with a dosage of 0.8 mg mL^{-1} and 0.3 mg mL^{-1} , respectively, of which both were slightly higher than the content of CN moiety and P25 moiety in CN@C-P25. A 300 W xenon lamp was utilized as the light source for photocatalytic NADH regeneration. The distance between the light source and the quartz cuvette was set as 10 cm, where the light intensity was around 1000 mW cm^{-2} . The concentration of NADH during the reaction was measured by a Hitachi U-3100 UV-visible spectrophotometer via Lambert-Beer Law with the molar absorption coefficients of $6220 \text{ cm}^{-1} \text{ M}^{-1}$. For the cycling experiment, the photocatalysts were collected by centrifugation, washed three times by DI water after each cycle. All other components except the photocatalysts

were fresh during each cycle.

2.4. Biomass as electron donor for photocatalytic NADH regeneration

Biomass like carbohydrate (e.g., glucose, xylose and fructose) and amino acid (e.g., cysteine and methionine) were chosen as the electron donors for NADH regeneration. The concentration of these electron donors was regulated in the range of $400\text{--}1000 \text{ mmol L}^{-1}$, and the pH was regulated in the range of 6.0–9.0. Other conditions were the same with the standard procedure of photocatalytic NADH regeneration. The electron donating ability was detected by testing the performance of photocatalytic NADH regeneration using a Hitachi U-3100 UV-visible spectrophotometer.

2.5. Characterizations

2.5.1. Ultraviolet photoelectron spectroscopy

Ultraviolet Photoelectron Spectroscopy (UPS) was measured by a K-Alpha⁺ equipment with an ultraviolet light (He I, 21.22 eV) as the excitation source. The photocatalysts were pressed into thin film for better contact between the sample and the instrument. Due to the low electrical conductivity of carbon nitride-based photocatalysts, a bias voltage of -10 V and a pass energy of -3 V were added to amplify the signal.

2.5.2. General characterizations

Scanning electron microscope (SEM) images were obtained with an FEI Nova XL430 and Hitachi Limited instrument. Transmission electron microscope (TEM) images and electron energy loss spectroscopy (EELS) were received by a FEI Tecnai G2 F20 equipment. Powder X-ray diffraction (XRD) was performed by using a Rigaku D/max 2500 V/PC instrument, and the data was obtained in the range of $5\text{--}60^\circ$ (2θ) with a rate of 6° min^{-1} . Fourier transform infrared spectroscopy (FT-IR) was carried out on a Nicolet-560 spectrometer. X-ray photoelectron spectroscopy (XPS) was measured on a PerkinElmer PHI 1600 ESCA. Raman spectroscopy was performed on a Renishaw inVia reflex spectrometer with 325 nm excitation. The excitation using lasers with 473 nm,

532 nm, 633 nm, and 785 nm all showed fluorescence signals much stronger than the Raman signals of samples. Solid-State NMR was carried out on a Bruker AVANCE NEO 400 WB spectrometer equipped with a 4 mm standard bore CPMAS probe head whose X channel was tuned to 100.62 MHz for ^{13}C measurement, using a magnetic field of 9.39 T at 297 K. High resolution Solid-State NMR experiment was carried out on Bruker Avance NEO 500 MHz spectrometer equipped with a 3.2 mm HXY triple-resonance MAS probe. One-dimensional (1D) ^{13}C magic-angle spinning (MAS) spectrum was acquired under spinrate of 20 kHz with 125 kHz high-power decoupling on proton channel. The UV-vis spectra and diffuse-reflectance spectroscopy (DRS) were collected on a Hitachi U-3010. Electrochemical experiments were conducted with a CHI760 electrochemical workstation. Electrodes were prepared on FTO glass by a drop-casting method using Nafion (5%) as the agglomerant. Photoluminescence (PL) spectroscopy was performed on a Horiba Jobin Yvon Fluorolog3 fluorescence spectrometer. Electron paramagnetic resonance (EPR) spectroscopy was carried out on a Bruker A300 EPR Spectrometer at a frequency of 9.837 GHz. Transient absorption (TA) was recorded on a Edinburgh LP980-KS Transient absorption spectrometer.

3. Results and discussion

3.1. Preparation and characterizations of the heterojunction photocatalysts

To prepare CN@C-P25, melamine and P25 nanoparticles (NPs) were mixed in DI water and then sonicated to obtain a well-dispersed suspension. TA solution was added to the suspension under vigorous stirring. The white suspension turned into light orange immediately due to

the formation of coating assemblies via the coordination reaction between TA and P25 on the surface of melamine. The obtained melamine@polyphenol-P25 composite transformed into the target heterojunction photocatalysts (CN@C-P25) after calcination. For control, CN-P25 and CN-C-P25 were prepared by calcining the physical mixture of melamine/P25 and melamine/TA/P25, respectively.

The chemical compositions and crystal structures of the heterojunction photocatalysts were examined. As shown in Fig. 1a, all CN-based photocatalysts exhibited similar FT-IR spectra of typical CN spectrum [43]. The absorption band at 810 cm^{-1} belonged to the breathing mode of the heterocycles, while the multi-absorption bands at $1100\text{--}1700\text{ cm}^{-1}$ were assigned to the stretching vibration of C-N heterocycles. The triplet bands at around 3200 cm^{-1} corresponded to the primary/secondary amine residues. As for P25, the absorption band from 400 cm^{-1} to 800 cm^{-1} in FT-IR spectrum belonged to the stretching vibration of Ti-O bond while the absorption band at around 1600 cm^{-1} was ascribed to the vibration of the adsorbed H_2O . The small humps of Ti-O stretching vibration at $400\text{--}550\text{ cm}^{-1}$ in CN-P25, CN-C-P25 and CN@C-P25 verified the loading of P25 on CN. The band at around 2400 cm^{-1} belonged to the surface absorbed CO_2 during the measurement. Typical XRD pattern of CN was obtained, where the peak at around 13.0° (100) corresponded to the in-plane structure of tri-s-triazine and the peak at around 27.2° was ascribed to the interlayer periodic stacking (Fig. 1b). P25 showed a mixture of anatase TiO_2 (primary, characteristic peak at 25.3° , PDF No. 21-1272, JCPDS) and rutile TiO_2 (secondary, characteristic peak at 27.4° , PDF No. 21-1276, JCPDS). In the heterojunction photocatalysts, both the peaks of CN and P25 could be clearly observed, verifying the formation of the CN and P25 composites.

The elements of C, N, Ti and O were observed from the full scan XPS

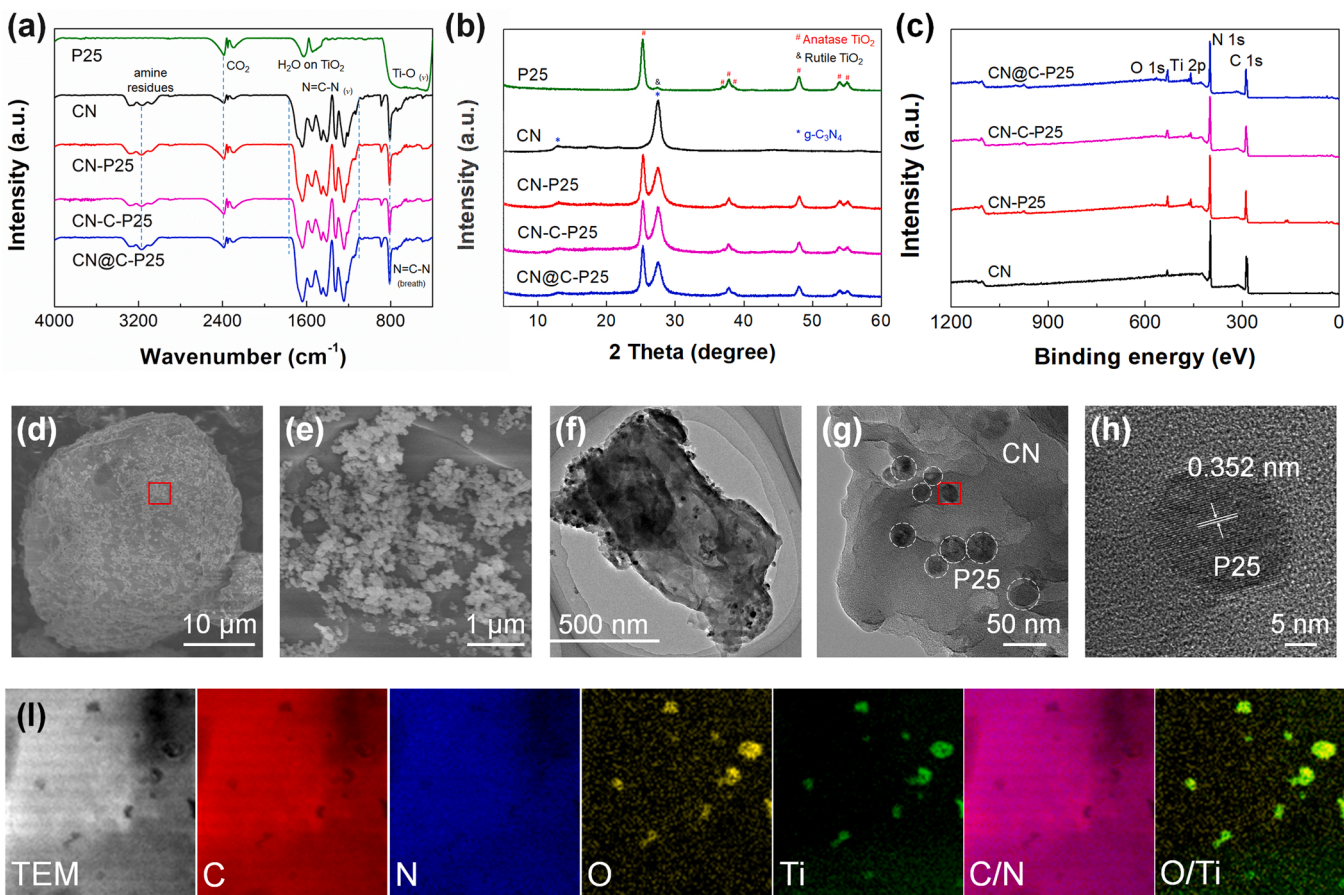


Fig. 1. (a) FT-IR spectra and (b) XRD patterns of P25, CN, CN-P25, CN-C-P25, and CN@C-P25; (c) XPS spectra of CN, CN-P25, CN-C-P25, and CN@C-P25; SEM images of (d) melamine@TA-P25 and (e) magnified area of the red square; (f, g) TEM images, (h) HRTEM image, and (i) EELS images of CN@C-P25.

spectra of all three samples (Fig. 1c). In the high-resolution C 1 s spectra (Fig. S1a), the peak of N-C≡N at 288.0 eV was originated from the aromatic C-N heterocycles. The peak at 284.6 eV in CN and CN-P25 was ascribed to the contaminated carbon. While in CN-C-P25 and CN@C-P25, the peak at 284.6 eV was a mixture of the contaminated carbon signal and C-C bond signal [44]. Compared with CN and CN-P25, both CN-C-P25 and CN@C-P25 exhibited higher C-C ratios (Table S1) due to the carbonization of extra carbon precursors. The N 1 s spectra exhibited typical CN peaks (Fig. S1b), including N-C≡N in the heterocycles (398.1 eV), the three tri-s-triazine joint of N-(C)₃ bond (399.8 eV) and the primary/secondary amine (-NH₂/-NH) residues (404.1 eV). As for Ti 2p XPS spectra (Fig. S1c), two peaks at 458.8 eV and 464.5 eV belonged to the Ti 2p_{3/2} and Ti 2p_{1/2} orbitals, respectively, which was consistent with TiO₂ [44]. The peak at 531.0 eV in O 1 s spectra was in the binding energy range of metal oxide (Fig. S1d). XPS spectra indicated successful construction of the heterojunction photocatalysts as well as successful incorporation of C moiety in CN-C-P25 and CN@C-P25.

Raman spectroscopy and ¹³C NMR were performed to investigate the carbon specie of our photocatalysts, CN@C-P25. As shown in Raman spectra (Fig. S2a), the peaks at 708.4 cm⁻¹, 760.3 cm⁻¹, 977.0 cm⁻¹, 1257.0 cm⁻¹ could be used to identify CN [45,46]. The D band at around 1340 cm⁻¹ and the G band at around 1560 cm⁻¹ were utilized to characterize the defect/edge carbon and sp² carbon in aromatic carbon, respectively. Pristine CN showed no D/G band signal. As for CN-P25, the signals of both D band and G band were a little difficult to distinguish from the background noise, indicating little C moiety was formed during preparation. CN@C-P25-50 with a moderate content of C moiety exhibited a slightly stronger D band signal and a small hump of G band, suggesting that the C moiety between CN and P25 was likely to be aromatic carbon with a few defects (like graphene fragments). CN@C-P25-200 with a higher content of C moiety demonstrated moderate D band and G band signals, indicating less defects in the aromatic carbon of CN@C-P25-200 than CN@C-P25-50. Then, ¹³C NMR was performed to investigate the C form in CN@C-P25 (Fig. S2b). Firstly, CN, CN-P25 and CN@C-P25-50 were measured and showed typical ¹³C NMR spectra of CN. The peak at δ = 156.6 ppm belonged to the internal carbon (C_i) of CN₃ while the peak at δ = 165.0 ppm was assigned to the edge carbon (C_e) of CN₂(NH_x) [47–49]. After increasing the content of C moiety and the resolution of solid-state NMR, a new peak at δ = 163.0 ppm appeared in CN@C-P25-200. The peak was in the range of C₆H₆ (110–170 ppm) while no other C species were located at this position, suggesting the formation of aromatic carbon [50]. According to the Raman and ¹³C NMR spectra, we could confirm that the C moiety in CN@C-P25 was aromatic carbon.

Afterwards, the morphologies of CN@C-P25 and the precursor of melamine@polyphenol-P25 were investigated. As shown in Fig. 1d, the surface of melamine was covered by a polyphenol-P25 layer, where P25 NPs could be seen clearly in the magnified image in Fig. 1e. After calcination, the CN@-C-P25 was obtained and characterized by TEM. As shown in Fig. 1f, g, P25 NPs were dispersedly anchored on CN sheets. The crystal structure of anatase TiO₂ were observed with a lattice of 0.352 nm, corresponding to the (101) crystal facet (Fig. 1h). Electron energy loss spectroscopy (EELS) was performed to explore the element distribution of CN@C-P25. An area of P25 NPs distributed CN sheet was selected (Fig. 1i). C and N elements were uniformly distributed on the CN sheet, while weak signals were found at the position of P25 NPs. In contrast, the signals of O and Ti elements were intensively dispersed at the position of P25 NPs. Weak signal of O element could also be seen on the CN sheet, which was ascribed to the partial oxidation of CN during calcination. Moreover, the position of dark holes in C/N composite image was consistent with the position of bright points of P25 NPs in O/Ti composite image. TEM images and EELS demonstrated the structure of CN@C-P25, where the P25 NPs were dispersedly spreaded over the CN sheets.

3.2. Optical and photoelectric properties of the heterojunction photocatalysts

The interfacial charge transfer was primarily dominated by two factors: the energy barrier and the interfacial contacting area. Firstly, the band structure of the heterojunction photocatalysts was analyzed to explore the variation of energy barrier at the heterojunction interfaces. UV-vis diffuse reflectance spectroscopy (DRS) was applied to probe the band structure of the heterojunction photocatalysts. Given the band gaps of CN and P25, the absorption at visible range was primarily contributed to the band-to-band absorption of CN. In Fig. 2a and S3, the absorption edge of CN was 460 nm with a corresponding band gap (Eg) of 2.70 eV. CN-P25 exhibited a slight red shift to 476 nm (Eg = 2.62 eV) compared with CN due to the formation of defects at CN/P25 interface during calcination. As for CN@C-P25, the absorption edge shifted to 496 nm with a narrower band gap of 2.53 eV. The tail absorption at longer wavelength was ascribed to the absorption of C moiety, where the energy was dissipated via heat instead of generating excited charges. Then, the valance band (VB) of the heterojunction photocatalysts was measured by XPS valance band spectra. Given the higher content of CN by contrast with P25, the VB shown in XPS spectra belonged to the subject material of CN. As demonstrated in Fig. 2b, c, the VB of CN located at 1.3 eV. The VB shifted 0.4 eV in CN-P25 (1.7 eV) compared with that in CN, while kept consistent in CN@C-P25. We could then deduce that the positive shift in CN-P25 was caused by the formation of Schottky contact between CN and P25. In contrast, when C moiety was introduced as the interface layer, the unaltered VB indicated that no band bending occurred at the interface. However, considering the narrowed band gap in DRS, a positive shift of CB in CN@C-P25 could be concluded.

Ultraviolet photoelectron spectroscopy (UPS) was further performed to investigate the band information more precisely. Due to the inherent non-uniformity of particulate sample, we could only obtain the relative position of Fermi level from UPS spectra. In Fig. 2c, an energy gap of 0.6 eV between Fermi level (FL) and vacuum level (VL) was observed in CN-P25, which was much higher than that of pristine CN. Combining with the XPS result, we could confirm that a 0.4 eV up-bending of CN in CN-P25 (Fig. 2d). Given the intrinsic rigid surface of the two semiconductors, the interface dipole could be ignored [51], indicating the energy difference was mainly ascribed to the band bending of two semiconductors. Therefore, a 0.2 eV down-bending of P25 could be deduced. The 0.4 eV up-bending resulted in the formation of Schottky contact at the CN/P25 interface, which restrained the electron transfer from CN to P25. CN-C exhibited a 0.66 eV larger energy gap compared with CN. The energy level of interfacial C moiety was equal to the Fermi level considering its excellent conductivity, which was similar to the situation of metal-semiconductor contact [17,22]. The hybridization between the aromatic C moiety and C p_z orbital in triazine of CN (the major contributor to the conduction band of CN [52]) resulted in a positive shift of 0.17 eV at CN/C interface instead of a band bending shown in CN-P25, while the position of VB was unchanged compared with CN. At the CN/C interface, electron transfer from CN to C moiety went through the delocalized π-π stacking between triazine and aromatic groups. Furthermore, CN@C-P25 exhibited a larger energy gap that was 0.1 eV higher than CN-C, indicating a 0.1 eV down-bending of P25 at C/P25 interface (Fig. 2d). Such a low energy barrier could be easily overcome by the excited electrons from CN. The interlayer of C switched the 0.4 eV Schottky contact to a 0.1 eV Ohmic contact in CN@C-P25 and eventually led to an easier interfacial charge transfer, which was also proved by photoluminescence (PL) spectroscopy with promoted charge separation (Fig. S4a) and reduced average fluorescent lifetime (Fig. S4b).

Subsequently, the interfacial contacting area of the heterojunction photocatalysts was evaluated. For control, another ternary heterojunction photocatalyst, CN-C-P25, with P25 randomly distributed on CN was prepared (Fig. 2e). The interfacial contacting area between CN and

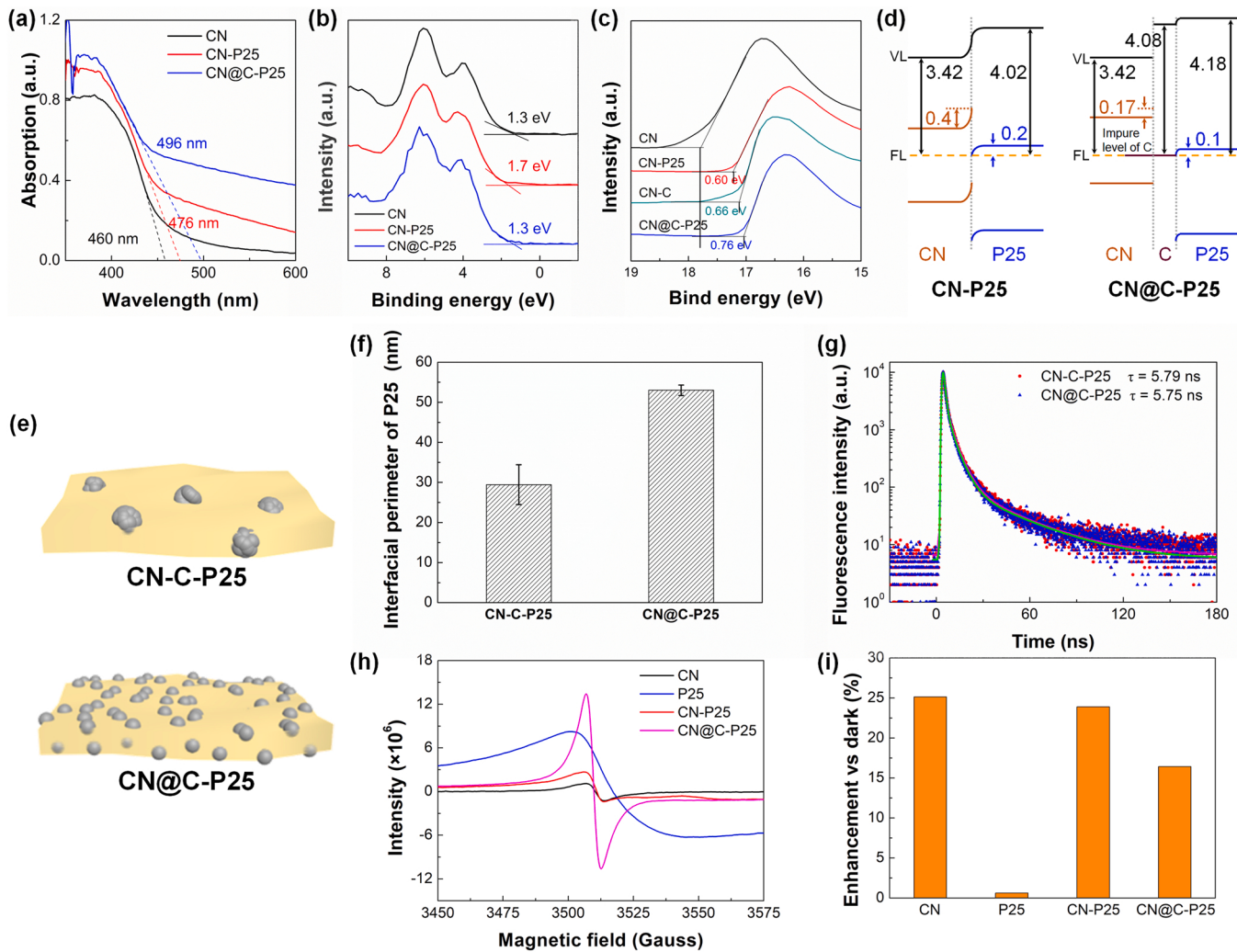


Fig. 2. (a) UV-vis DRS and (b) XPS valence band spectra of CN, CN-P25, and CN@C-P25. (c) UPS spectra of CN, CN-P25, CN-C, and CN@C-P25. (d) Schematic diagram of energy level in CN-P25 and CN@C-P25. (e) Scheme of CN-C-P25 and CN@C-P25. (f) Average perimeter between CN and single P25 particle in CN-C-P25 and CN@C-P25. (g) Time-resolved photoluminescence spectra of CN-C-P25 and CN@C-P25. (h) EPR spectra of CN, P25, CN-P25 and CN@C-P25 under dark. (i) Enhancement of EPR signals after light irradiation of CN, P25, CN-P25 and CN@C-P25.

P25 in CN-C-P25 and CN@C-P25 was calculated through measuring the effective perimeter of the boundaries between CN and P25 in TEM images (Fig. S5). The average effective perimeter of P25 surrounded by CN was calculated as 53.0 nm and 29.5 nm for CN@C-P25 and CN-C-P25, respectively (Fig. 2f). The equivalent radius of P25 was 8.44 nm and 4.70 nm, respectively, of which the former in CN@C-P25 was close to the radius of P25 NPs of 10 nm. Accordingly, the interfacial contacting area was estimated as 895.1 nm^2 per particle for CN@C-P25 and 277.6 nm^2 per particle for CN-C-P25, respectively, considering P25 as an ideal sphere. Therefore, a 3.2-fold enhancement of interfacial contacting area was obtained when P25 was well distributed. Notably, a similar charge transfer ability of CN@C-P25 and CN-C-P25 was observed by PL (Fig. 2g) with almost the same average fluorescent lifetime.

EPR spectra were performed to explore the electron transfer processes in CN, P25, CN-P25 and CN@C-P25. The spectra of each sample were taken under dark as well as under 3-min visible light irradiation ($\geq 420 \text{ nm}$). As shown in Fig. S6, all CN based samples exhibited a single Lorentzian line with a g value of ~ 2.0019 , which could be assigned to the unpaired electron on carbon atoms of the aromatic rings within π -bonded nanosized clusters [53,54]. In Fig. S6b, the single Lorentzian line with a g value of 1.9984 belonged to the unpaired electron on Ti(III) species in P25 [55,56]. CN-P25 also exhibited a mixture signal of CN and P25 (Fig. S6c). As for CN@C-P25, a stronger single Lorentzian line was

observed (Fig. 2h). The presence of C moiety improved the π - π stacking between tri-s-triazine unit and aromatic carbon, stabilizing the unpaired electron via delocalization. Thus, the quantity of the unpaired electrons was enhanced as well as the EPR signal. After visible-light irradiation, P25 showed no response with a constant EPR signal (Fig. S6b). The signals enhancement of P25 (0.629%) was assigned to the error of baseline. As for CN based materials, the enhancement of EPR signals primarily located at around $g = 2.0019$. We could then conclude that the signal variation was mainly determined by the quantity of unpaired electrons in CN. As shown in Fig. 2i, CN exhibited an enhancement of 25.1% compared with its dark signal, while the enhancements of CN-P25 and CN@C-P25 were 23.9% and 16.4%, respectively. After the formation of heterojunction between CN and P25, the photo-excited electrons were transferred from CN to P25, weakening the EPR signal of unpaired electron in CN. The slightly reduced enhancement of CN-P25 compared with CN indicated a small quantity of electrons being transferred to P25 due to the hindrance of Schottky barrier between CN and P25. On the contrary, the obvious reduced enhancement of CN@C-P25 compared with CN indicated a large quantity of electrons being transferred away from CN to P25. Considering the formation of the Ohmic contact between CN and P25 after introducing C moiety, we confirmed that the C moiety could facilitate the electron transfer from CN to P25.

To finally investigate the influence of energy barrier and interfacial contacting area on the charge transfer, photoelectrochemical measurement was conducted (Fig. 3a). Firstly, EIS Nyquist plots were performed to analyze the interfacial resistance at the interface. As shown in Fig. 3b, CN exhibited the smallest resistance. The fabrication of CN-P25 heterojunction increased the resistance due to the formation of CN/P25 interface. CN-C-P25 exhibited a slightly decreased resistance compared with CN-P25, which was a trade-off between reduced interfacial energy barrier and limited interfacial contacting area. As for CN@C-P25, an obvious decrease of resistance was observed, which could be ascribed to the enlarged interfacial contacting area compared with CN-C-P25. The overall charge transfer flux was then measured by photocurrent response. As shown in Fig. 3c, the photocurrent density of CN-P25 was 1.8-fold higher than that of CN due to the facilitated charge separation by the heterojunction structure. When directly introducing C moiety as the interlayer, CN-C-P25 only exhibited negligible increase of photocurrent density (2.1-fold of CN) compared with CN-P25 due to its much lower interfacial contacting area for charge transfer. In sharp contrast, for CN@C-P25, the photocurrent density was remarkably enhanced (4.5-fold of CN). Different from CN-C-P25, the pre-assembly of TA-P25 layer on the surface of melamine created more effective interfacial contacting area to facilitate interfacial charge transfer, leading to an enhancement of overall charge transfer flux. To acquire an in-depth understanding of the difference in charge transfer flux of the samples, voltammogram under chopped light irradiation was also performed to measure the charge density (Fig. 3d). By using a fast electron quencher of methyl viologen dichloride (MVCl_2), the charge transfer rate of photocatalysts could be accelerated to a similar level owing to a promoted extraction of photogenerated electrons by the electrolyte. The photocurrent onset potential in a voltammogram was equal to the quasi-Fermi level of majority carriers (electrons). The carrier density ratio between different photocatalysts could be then calculated by the quasi-Fermi level via Nernst Eq. (1) [57]:

$$E_{f1} - E_{f2} = kT \ln \left(\frac{N_f1}{N_f2} \right) / e \quad (1)$$

where E_f was the quasi-Fermi level (V), k was the Boltzmann's Constant (J/K), T was the temperature (K), N_f was the carrier density, and e was the elementary charge (eV). The carrier density of CN-P25, CN-C-P25 and CN@C-P25 was 2.18-fold, 1.48-fold, and 4.75-fold higher than that of CN, respectively. The carrier density of CN-C-P25 was lower than that of CN-P25 under similar charge transfer ability due to the aggregation of C moiety that increased the invalid light absorption and, thereby, contributed little to the generation of excited electron-hole pairs. The remarkable improvement of carrier density of CN@C-P25 could be benefited from reduced energy barrier, enlarged interfacial contacting area, and the less aggregated C moiety, significantly alleviating the non-ideal interfacial effects.

3.3. Photocatalytic NADH regeneration

The schematic processes and performance of photocatalytic NADH regeneration and photo-enzyme-coupled artificial photosynthesis were shown in Fig. 4a. Among the prepared photocatalysts, CN@C-P25 exhibited the highest activity with a NADH yield of 77.3% (Fig. 4b). The activity of P25 with a yield of 13.2% was the lowest among the photocatalysts due to the weak absorption of visible light. The low yield of CN (27.3%) was ascribed to the fast charge recombination in bulk materials. The heterojunction photocatalyst, CN-P25, exhibited an improved yield (58.2%) compared with CN and P25 due to the promoted charge separation, which was also higher than the sum of the yield of CN and P25. When the third moiety of C was introduced, the yield was further elevated to 70.7% in CN-C-P25 and 77.3% in CN@C-P25 with initial reaction rates of $4244 \mu\text{mol h}^{-1} \text{g}^{-1}$ and $5185 \mu\text{mol h}^{-1} \text{g}^{-1}$, respectively (Fig. 4c). The recycling stability of CN@C-P25 was then explored. After 10 cycles, the yield of NADH regeneration was almost the same to the first cycle, indicating the superior recyclability of

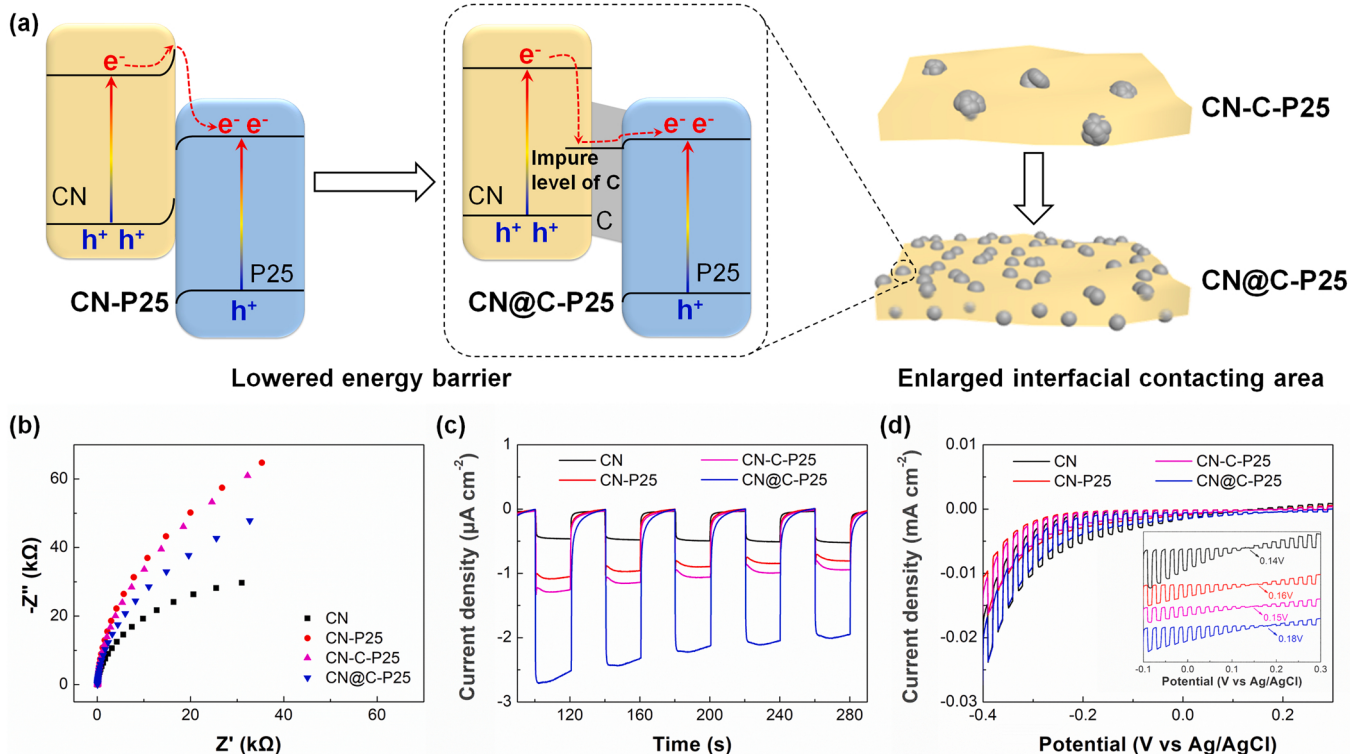


Fig. 3. (a) Interface engineering of CN@C-P25 with lowered energy barrier and enlarged interfacial contacting area. (b) EIS spectra, (c) photocurrent response, and (d) charge carrier density of CN, CN-P25, CN-C-P25, and CN@C-P25.

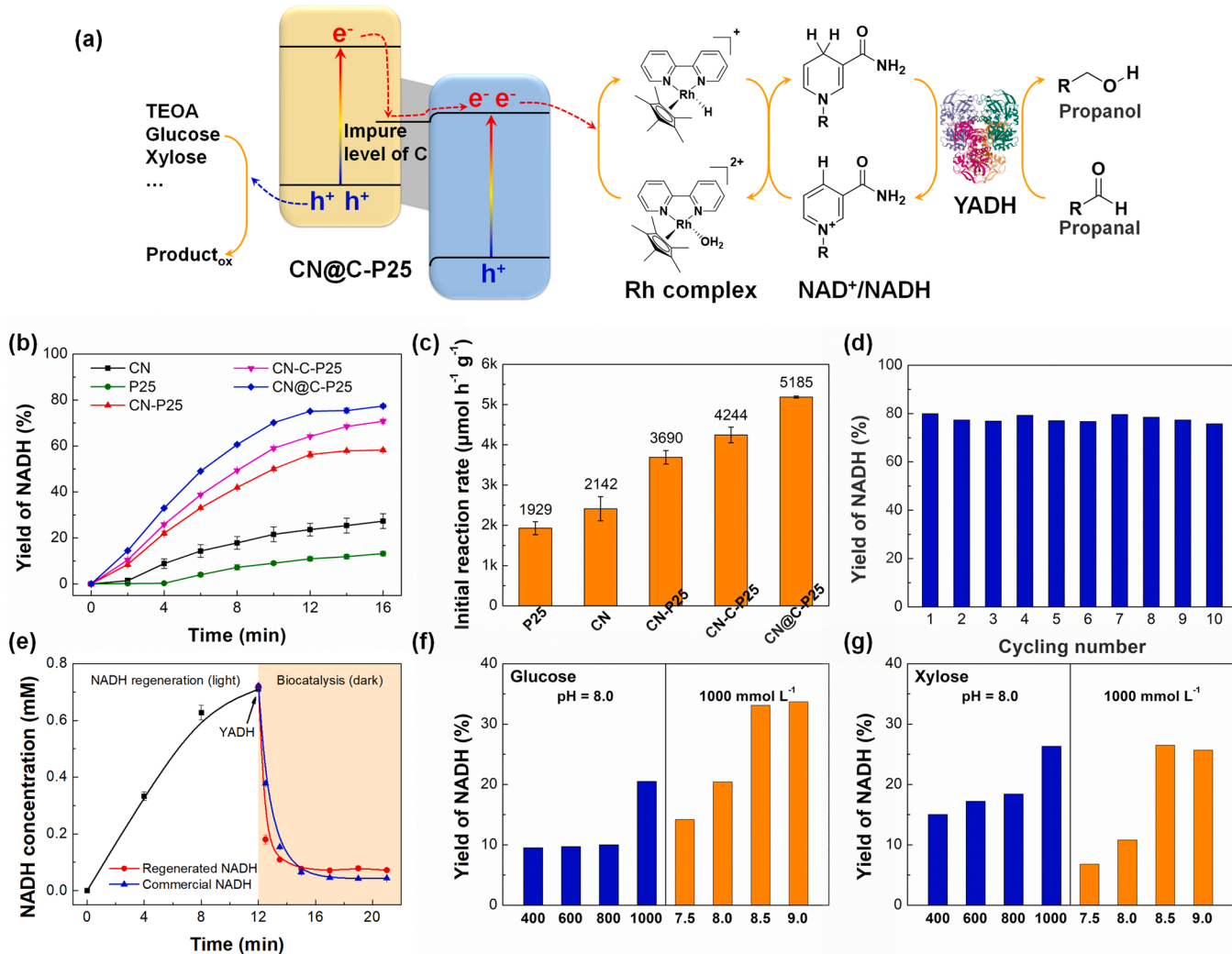


Fig. 4. (a) Scheme of photocatalytic NADH regeneration photo-enzyme coupling artificial photosynthesis. (b) NADH regeneration activity and (c) corresponding initial reaction rate of CN, P25, CN-P25, CN-C-P25, and CN@C-P25. Dosage of photocatalysts: 0.8 mg mL⁻¹ of CN, 0.3 mg mL⁻¹ of P25, 1.0 mg mL⁻¹ of CN-P25, CN-C-P25 and CN@C-P25. The dosage of CN and P25 was slightly higher than the content of CN moiety and P25 moiety in CN@C-P25, respectively. (d) Cycling stability of CN@C-P25. (e) Selectivity validation of photocatalytic regenerated 1, 4-NADH. (f, g) Photocatalytic NADH regeneration by biomass: (f) by glucose and (g) by xylose under varied pH value and concentration of the electron donor.

CN@C-P25 (Fig. 4d). The enzymatic reactivity of the regenerated NADH was then verified. As shown in Fig. 4e, NADH was first generated through photocatalytic reaction. Then, alcohol dehydrogenase from *Saccharomyces cerevisiae* and propionaldehyde were added to consume the generated NADH. Meanwhile, commercial NADH with the same concentration was also used for enzymatic consumption. Regenerated NADH exhibited similar reaction tendency compared with commercial NADH, indicating the successful regeneration of enzyme-active 1, 4-NADH. Furthermore, the sacrificial electron donor of TEOA was replaced by the structural unit of biomass, including carbohydrates and amino acids, for a greener route of photocatalytic NADH regeneration. The utilization of biomass can provide an alternative solution to the insufficient driving force in photocatalytic NADH regeneration when using H₂O as the electron donor. Among the biomass, glucose and xylose exhibited potential substitutability to TEOA with an optimal NADH yield of 33.7% and 26.5%, respectively (Fig. 4f, g and S7). The activity could be further increased when the reaction occurred under nitrogen atmosphere (Fig. S8). Such attempt indicates the possibility of using lignocellulose as the electron donor to power photocatalytic NADH regeneration [58].

The regeneration of NADH required a Rh complex as the co-catalyst to guarantee the selectivity of 1, 4-NADH. The electron transfer from the

photocatalyst to the co-catalyst also influence the efficiency of NADH regeneration. Transient absorption spectroscopy was performed to analyze the electron transfer between CN@C-P25 and Rh complex. The electron transfer efficiency was calculated based on Eq. (2) [59]:

$$\varphi_{ET} = 1 - \frac{k_0}{k_{obs}} \quad (2)$$

where φ_{ET} was electron transfer efficiency, $k_0 = 1/t_{50\%}$ was without co-catalyst and $k_{obs} = 1/t_{50\%}$ was with co-catalyst (s⁻¹). In Fig. S9a, b, the ΔOD gradually declined with increasing the concentration of Rh. The electron transfer efficiency calculated by Eq. (2) was related to the concentration of Rh (Fig. S9c). Accordingly, 1 $\mu\text{mol L}^{-1}$ of Rh complex was sufficient to accept the electrons from the photocatalysts (0.2 mg mL⁻¹). The amount of Rh we used in the experiment (200 $\mu\text{mol L}^{-1}$ Rh for 1.0 mg mL⁻¹ photocatalysts) was excessive for the reaction, indicating the activity of NADH regeneration was dominated by the photocatalyst matrix.

3.4. Elucidation of interfacial charge transfer in CN@C-P25

The C moiety played a critical role in regulating the energy barrier and interfacial contacting area for charge transfer. Therefore, we

adjusted C moiety by altering the amount of TA precursor to explore the charge transfer behaviors in CN@C-P25. The photocatalytic NADH regeneration activities of CN@C-P25-X were measured, where X mg of TA was added during their preparation. In Fig. 5a, CN@C-P25-50 exhibited the highest activity with a yield of 75.5%. CN@C-P25-10 and CN@C-P25-100 exhibited similar activities (yield of ca. 63.5%), while CN@C-P25-200 revealed the lowest yield of 57.1%. Firstly, when a small amount of C moiety was introduced, only part of interface between CN and P25 was covered by the C moiety, leading to a moderate activity. When TA was increased to 50 mg, the amount of TA was sufficient to coordinate with all P25 NPs for maximizing the interfacial contacting area. Further increasing the amount of TA would lead to the self-aggregation of C moiety. The non-photoresponse specie would cause the increase of the invalid light absorption. Thus, CN@C-P25-100 and CN@C-P25-200 exhibited the decreased activities compared with CN@C-P25-50.

To verify the hypothesis, we first performed voltammogram measurement to obtain the charge density and charge carrier lifetime, respectively. As shown in Fig. 5b, the quasi-Fermi levels of CN@C-P25-10, CN@C-P25-50, g-CN@C-P25-100 and CN@C-P25-200 were 0.14 V, 0.22 V, 0.15 V and 0.11 V, respectively. Accordingly, the charge density of these heterojunction photocatalysts followed this order: CN@C-P25-50 > CN@C-P25-100 > CN@C-P25-10 > CN@C-P25-200. When smaller amount of TA was used to fabricate CN@C-P25, the lower interfacial contacting area was the primary restriction. While excessive amount of TA would lead to the formation of the self-aggregated C moiety, causing some invalid light absorption. A proper amount of TA endowed the photocatalysts with the optimal interfacial contacting area, low energy barrier and moderate light absorption, thus acquiring the highest activity. Then, tr-PL spectroscopy was performed to evaluate the charge transfer. As shown in Fig. 5c, CN@C-P25-10, CN@C-P25-50 and CN@C-P25-100 exhibited similar charge carrier lifetime of ca. 5.75 ns while CN@C-P25-200 exhibited a much longer lifetime of 11.90 ns. The unaltered charge transfer ability from CN@C-P25-10 to CN@C-P25-100 indicated the excellent interfacial contact and charge transfer abilities of TA-derived C moiety. However, excessive addition of TA would hinder the charge transfer due to the formation of bulk C moiety. Briefly, the strong metal coordination and remarkable surface coating abilities of polyphenols could create low energy barrier between P25 and CN in a broad range. The amount of TA mainly affected the effective interfacial contacting area formed in-between. Optimization of the morphological and photoelectric properties of the interface was thus realized in a facile way.

3.5. Discussion

To address the non-ideal interfacial effects, we construct CN@C-P25 ternary heterojunction photocatalysts to simultaneously lower the interfacial energy barrier and enlarge the interfacial contacting area.

Considering the preparation process using polyphenols of tannic acid as both the linker of CN and P25 and the carbon source of C moiety, as well as the XRD, FT-IR, XPS, SEM and TEM results, we could conclude that the P25 nanoparticles are well dispersed on CN sheets and surrounded by the C moiety in CN. Raman and ^{13}C NMR spectra indicate the specie of C moiety is aromatic carbon, which could potentially promote the charge transfer between CN and C via π - π stacking interaction between tri-s-triazine and aromatic carbon.

To verify the hypothesis of lowering the interfacial energy barrier, we first measure the band structure of a series of photocatalysts through DRS, XPS and UPS technologies. The results indicated that the directly construction of CN-P25 heterojunction would lead to an unfavorable band bending due to the mismatching of Fermi level of the two catalysts. A 0.4 eV Schottky barrier is formed, which slows down the interfacial charge transfer. When the C moiety is in-situ introduced to the skeleton of CN as a intermediary between CN and P25, the π - π stacking of aromatic C moiety and CN facilitates the electron transfer from CN to P25 according to the EPR spectra. Meanwhile, the Fermi level of aromatic C and P25 both located at around 0 eV_{NHE}. As a result, an 0.1 eV Ohmic contact is formed between CN and P25 after introducing the C moiety, where the electrons generated on CN are firstly transferred to C moiety via π - π stacking interaction and easily climb the 0.1 eV Ohmic barrier to reach P25, realizing the spital charge separation. The improvement of charge separation in CN@C-P25 by contrast with CN-P25 to is directly confirmed by PL and tr-PL spectroscopy.

As for the hypothesis of enlarged interfacial contacting area, we perform TEM test to count the number of P25 on CN, calculating the effective diameter of P25 as well as the interfacial contacting area between CN and P25. P25 in CN@C-P25 exhibits a diameter (8.44 nm) close to P25 NPs (10 nm), indicating a nearly monodispersed P25 on CN. P25 in CN-C-P25, on the contrary, demonstrates an apparent aggregation on TEM images and a much smaller effective diameter (4.70 nm) than P25 NPs. The randomly distributed P25 on CN in CN-C-P25 only leads to an effective interfacial contacting area of 277.6 nm² per particle, which is less than one third of CN@C-P25 with well distributed P25 on CN (895.1 nm² per particle).

Then, photoelectrochemical measurement is performed to further verify the relationship between structure and electron transfer performance. From EIS spectra, we find that the formation of heterojunction between CN and P25 results in the increase of the overall resistance of the material compared with pristine CN, which is mainly derived from the CN/P25 interface, confirming the formation of the Schottky barrier. The incorporation of C moiety in CN@C-P25 remarkably reduces the resistance, which could be ascribed to the formation of the Ohmic contact, lowering the interfacial resistance between CN and P25. However, CN-C-P25 only demonstrates a slightly reduced resistance compared with CN-P25, suggesting that the limited interfacial contacting area possesses a negative effect on electron transfer. The chopped photocurrent reflects the overall performance of generating

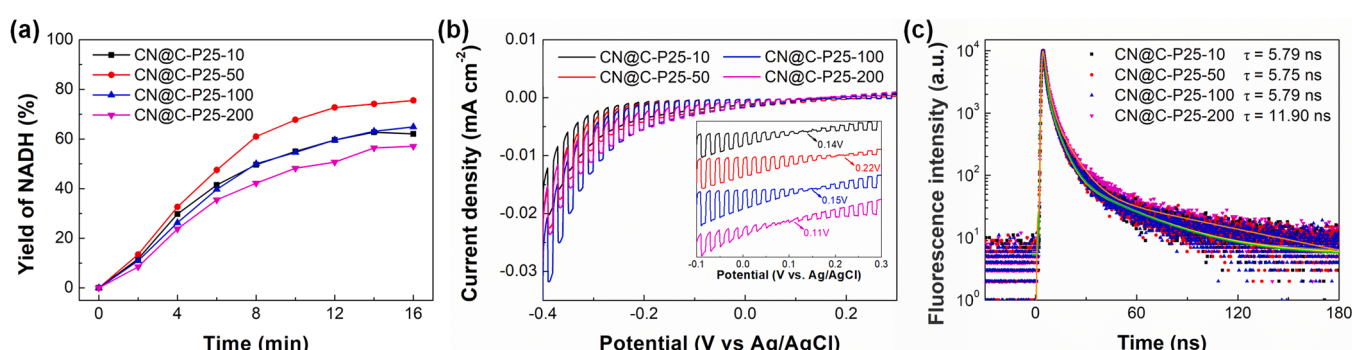


Fig. 5. (a) Photocatalytic NADH regeneration activity, (b) charge carrier density, (c) time-resolved PL spectra its simulation curve of CN@C-P25-X, where X stands for the precursor of TA added during preparation.

photoresponse charge carriers. The photocurrent of CN-P25 (1.8-fold to CN) increases due to the formed heterojunction that promotes the spital charge separation. The moderate increase of photocurrent in CN-C-P25 (2.1-fold to CN) compared with CN-P25 is the trade-off result between reduced interfacial energy barrier and limited interfacial contacting area. CN@C-P25 (4.5-fold to CN) exhibited an obvious enhancement of photocurrent, which is ascribed to a multiplying effect of simultaneously lowering the interfacial energy barrier and enlarging the interfacial contacting area. The charge carrier density is then calculated by positioning the onset potential during LSV measurement with electron quenchers. The construction of heterojunction improves the charge carrier density compared with pristine CN. Creating a ternary heterojunction with limited interfacial contacting area plays a negative effect on charge carrier density compared with CN-P25 due to the electron quenchers vastly weaken the charge recombination in CN-P25. Only by enlarging the effective interfacial contacting area as well as lowering the interfacial energy barrier, we could obtain a further increase of charge carrier density for catalysis.

The activity of photocatalytic NADH regeneration is mainly determined by the density of surface electrons. The co-catalyst, Rh complex, is proved to be excess in our system by TA spectroscopy. Therefore, the diffusion of Rh complex and the communication between Rh complex and NADH may not be the rate-limiting step, especially under low density of surface electrons. The NADH activity exhibits a similar tendency with photocurrent density with an order of CN@C-P25 > CN-C-P25 > CN-P25 > CN. The enhancement of activity is smaller than that of the photocurrent when comparing CN@C-P25 and CN-C-P25, which is probably influenced by two factors: the limitation of substrate diffusion under high surface electron density and the reaction equilibrium of NADH regeneration. The content of C moiety could further reflect the relationship between structure and performance. A less content of C moiety results in a smaller effective interfacial contacting area as well as decreased photocatalytic activity. An excess content of C moiety leads to the formation of bulk C moiety, which instead hinders the interfacial charge transfer. Regulating the interfacial charge transfer and interfacial contacting area to achieve a win-win situation is critical to optimize the overall photocatalytic activity.

4. Conclusions

In summary, we demonstrate a facile strategy to suppress the non-ideal interfacial effects toward high-efficient charge transfer in heterojunction photocatalysts. Two typical semiconductors, graphitic carbon nitride (CN) and titania (P25) were utilized to construct an organic-inorganic heterojunction via the assistance of polyphenols. The CN@C-P25 photocatalysts exhibited a 2.5-fold enhancement of charge transfer flux owing to the simultaneous optimization of interfacial energy barrier and interfacial contacting area. Specifically, the uniform dispersion of P25 on CN assembled by polyphenols elevated the interfacial contacting area of 3.2 folds and the spontaneous transformation of polyphenols to conjugated C moiety facilitated the π - π stacking interfacial charge transfer by switching a 0.4 eV Schottky contact to a 0.1 eV Ohmic contact. The strong metal coordination ability and universal surface coating property of polyphenols expands the toolbox of interface construction. Our study affords a general strategy to suppress the non-ideal interfacial effects in heterojunction photocatalysts and sheds some light on rational engineering of the interface in energy-transfer related applications.

CRediT authorship contribution statement

Yizhou Wu: Conceptualization, Methodology, Formal analysis, Investigation, Writing – original draft, Writing – review & editing, Visualization. **Yu Chen:** Validation, Formal analysis, Investigation, Writing – review & editing, Visualization. **Donglin Li:** Validation, Formal analysis, Investigation. **Dania Sajjad:** Validation, Investigation.

Xixuan Chen: Validation, Investigation. **Yiying Sun:** Writing – review & editing. **Shusong Liu:** Writing – review & editing. **Jiafu Shi:** Conceptualization, Methodology, Resources, Writing – review & editing, Supervision, Project administration, Funding acquisition. **Zhongyi Jiang:** Conceptualization, Resources, Writing – review & editing, Supervision, Project administration, Funding acquisition.

Declaration of Competing Interest

The authors declare that they have no known competing financial interests or personal relationships that could have appeared to influence the work reported in this paper.

Acknowledgment

The authors thank Dr. Xingyu Lu from Instrumentation and Service Center for Molecular Sciences at Westlake University for ^{13}C NMR measurement/data interpretation. This work is supported by the National Key Research and Development Program of China, China (2020YFA0907902), National Outstanding Youth Science Fund Project of National Natural Science Foundation of China, China (22122809), National Natural Science Foundation of China, China (21621004), Natural Science Foundation of Tianjin, China (19JCYBJC19700) and Open Funding Project of the State Key Laboratory of Biochemical Engineering, China (2020KF-06).

Author contributions

[†]Yizhou Wu and [‡]Yu Chen contributed equally. The manuscript was completed through contributions of all authors. All authors have given approval to the final version of the manuscript.

Supplemental information

The following files are available free of charge. Supplementary figures included High resolution XPS spectra, Raman spectra, ^{13}C NMR spectra, DRS spectra, PL spectra, TEM images, EPR spectra, photocatalytic NADH regeneration using glucose and xylose as the electron donor, photocatalytic NADH regeneration using glucose with/without protective gas of nitrogen, electron transfer efficiency from photocatalysts to co-catalysts calculated by transient absorption spectra.

Appendix A. Supporting information

Supplementary data associated with this article can be found in the online version at doi:10.1016/j.apcatb.2022.121261.

References

- [1] B. Zhang, L. Sun, Artificial photosynthesis: opportunities and challenges of molecular catalysts, Chem. Soc. Rev. 48 (2019) 2216–2264, <https://doi.org/10.1039/c8cs00897c>.
- [2] N. Kornienko, J.Z. Zhang, K.K. Sakimoto, P. Yang, E. Reisner, Interfacing nature's catalytic machinery with synthetic materials for semi-artificial photosynthesis, Nat. Nanotechnol. 13 (2018) 890–899, <https://doi.org/10.1038/s41565-018-0251-7>.
- [3] Y. Tachibana, L. Vayssières, J.R. Durrant, Artificial photosynthesis for solar water-splitting, Nat. Photonics 6 (2012) 511–518, <https://doi.org/10.1038/nphoton.2012.175>.
- [4] W.J. Ong, L.L. Tan, Y.H. Ng, S.T. Yong, S.P. Chai, Graphitic carbon nitride ($\text{g-C}_3\text{N}_4$)-based photocatalysts for artificial photosynthesis and environmental remediation: are we a step closer to achieving sustainability? Chem. Rev. 116 (2016) 7159–7329, <https://doi.org/10.1021/acscchemrev.6b00075>.
- [5] S. Chu, A. Majumdar, Opportunities and challenges for a sustainable energy future, Nature 488 (2012) 294–303, <https://doi.org/10.1038/nature11475>.
- [6] A. Hagfeldt, G. Boschloo, L.C. Sun, L. Kloo, H. Pettersson, Dye-sensitized solar cells, Chem. Rev. 110 (2010) 6595–6663, <https://doi.org/10.1021/cr900356p>.
- [7] M. Jeong, I.W. Choi, E.M. Go, Y. Cho, M. Kim, B. Lee, S. Jeong, Y. Jo, H.W. Choi, J. Lee, J.H. Bae, S.K. Kwak, D.S. Kim, C. Yang, Stable perovskite solar cells with efficiency exceeding 24.8% and 0.3-V voltage Loss, Science 369 (2020) 1615–1620, <https://doi.org/10.1126/science.abb7167>.

- [8] M. Faraji, M. Yousefi, S. Yousefzadeh, M. Zirak, N. Naseri, T.H. Jeon, W. Choi, A. Z. Moshfegh, Two-dimensional materials in semiconductor photoelectrocatalytic systems for water splitting, *Energy Environ. Sci.* 12 (2019) 59–95, <https://doi.org/10.1039/c8ee00886h>.
- [9] V. Andrei, B. Reuillard, E. Reisner, Bias-free solar syngas production by integrating a molecular cobalt catalyst with perovskite-BiVO₄ tandems, *Nat. Mater.* 19 (2020) 189–194, <https://doi.org/10.1038/s41563-019-0501-6>.
- [10] Q. Wang, K. Domen, Particulate photocatalysts for light-driven water splitting: mechanisms, challenges, and design strategies, *Chem. Rev.* 120 (2020) 919–985, <https://doi.org/10.1021/acs.chemrev.9b00201>.
- [11] Q. Wang, T. Hisatomi, Q. Jia, H. Tokudome, M. Zhong, C. Wang, Z. Pan, T. Takata, M. Nakabayashi, N. Shibata, Y. Li, I.D. Sharp, A. Kudo, T. Yamada, K. Domen, Scalable water splitting on particulate photocatalyst sheets with a solar-to-hydrogen energy conversion efficiency exceeding 1%, *Nat. Mater.* 15 (2016) 611–615, <https://doi.org/10.1038/NMAT4589>.
- [12] M.M. Lee, J. Teuscher, T. Miyasaka, T.N. Murakami, H.J. Snaith, Efficient hybrid solar cells based on meso-superstructured organometal halide perovskites, *Science* 338 (2012) 643–647, <https://doi.org/10.1126/science.1228604>.
- [13] J.X. Low, J.G. Yu, M. Jaroniec, S. Wageh, A.A. Al-Ghamdi, Heterojunction photocatalysts, *Adv. Mater.* 29 (2017), 1601694, <https://doi.org/10.1002/adma.201601694>.
- [14] Y. Wu, J. Shi, D. Li, S. Zhang, B. Gu, Q. Qiu, Y. Sun, Y. Zhang, Z. Cai, Z. Jiang, Synergy of electron transfer and electron utilization via metal-organic frameworks as an electron buffer tank for nicotinamide regeneration, *ACS Catal.* 10 (2020) 2894–2905, <https://doi.org/10.1021/acscatal.9b05240>.
- [15] K.B. Lin, J. Xing, L.N. Quan, F.P.G. De Arquer, X.W. Gong, J.X. Lu, L.Q. Xie, W. J. Zhao, D. Zhang, C.Z. Yan, W.Q. Li, X.Y. Liu, Y. Lu, J. Kirman, E.H. Sargent, Q. H. Xiong, Z.H. Wei, Perovskite light-emitting diodes with external quantum efficiency exceeding 20 per cent, *Nature* 562 (2018) 245–248, <https://doi.org/10.1038/s41586-018-0575-3>.
- [16] J. Du, F. Li, L. Sun, Metal-organic frameworks and their derivatives as electrocatalysts for the oxygen evolution reaction, *Chem. Soc. Rev.* 50 (2021) 2663–2695, <https://doi.org/10.1039/d0cs01191f>.
- [17] Z. Zhang, J.T. Yates, Band bending in semiconductors: chemical and physical consequences at surfaces and interfaces, *Chem. Rev.* 112 (2012) 5520–5551, <https://doi.org/10.1021/cr300626>.
- [18] D. Kim, K. Yong, Boron doping induced charge transfer switching of a C₃N₄/ZnO photocatalyst from Z-scheme to type II to enhance photocatalytic hydrogen production, *Appl. Catal. B Environ.* 282 (2021), 119538, <https://doi.org/10.1016/j.apcatb.2020.119538>.
- [19] Y.J. Zhang, T. Mori, L. Niu, J.H. Ye, Non-covalent doping of graphitic carbon nitride polymer with graphene: controlled electronic structure and enhanced optoelectronic conversion, *Energy Environ. Sci.* 4 (2011) 4517–4521, <https://doi.org/10.1039/c1ee01400e>.
- [20] M. Jourshabani, M.R. Asrami, B.K. Lee, An efficient and unique route for the fabrication of highly condensed oxygen-doped carbon nitride for the photodegradation of synchronous pollutants and H₂O₂ production under ambient conditions, *Appl. Catal. B Environ.* 302 (2022), 120839, <https://doi.org/10.1016/j.apcatb.2021.120839>.
- [21] L.L. Liu, F. Chen, J.H. Wu, M.K. Ke, C. Cui, J.J. Chen, H.Q. Yu, Edge electronic vacancy on ultrathin carbon nitride nanosheets anchoring O₂ to boost H₂O₂ photoproduction, *Appl. Catal. B Environ.* 302 (2022), 120845, <https://doi.org/10.1016/j.apcatb.2021.120845>.
- [22] Q. Wang, T. Hisatomi, Y. Suzuki, Z. Pan, J. Seo, M. Katayama, T. Minegishi, H. Nishiyama, T. Takata, K. Seki, A. Kudo, T. Yamada, K. Domen, Particulate photocatalyst sheets based on carbon conductor layer for efficient Z-scheme pure-water splitting at ambient pressure, *J. Am. Chem. Soc.* 139 (2017) 1675–1683, <https://doi.org/10.1021/jacs.6b12164>.
- [23] Q.J. Xiang, J.G. Yu, M. Jaroniec, Graphene-based semiconductor photocatalysts, *Chem. Soc. Rev.* 41 (2012) 782–796, <https://doi.org/10.1039/c1cs15172j>.
- [24] J.W. Fu, J.G. Yu, C.J. Jiang, B. Cheng, g-C₃N₄-based heterostructured photocatalysts, *Adv. Energy Mater.* 8 (2018), 1701503, <https://doi.org/10.1002/aenm.201701503>.
- [25] L. Jiang, X. Yuan, Y. Pan, J. Liang, G. Zeng, Z. Wu, H. Wang, Doping of graphitic carbon nitride for photocatalysis: a review, *Appl. Catal. B Environ.* 217 (2017) 388–406, <https://doi.org/10.1016/j.apcatb.2017.06.003>.
- [26] H. Kasap, R. Godin, C. Jeay-Bizot, D.S. Achilleos, X. Fang, J.R. Durrant, E. Reisner, Interfacial engineering of a carbon nitride-graphene oxide-molecular Ni catalyst hybrid for enhanced photocatalytic activity, *ACS Catal.* 8 (2018) 6914–6926, <https://doi.org/10.1021/acscatal.8b01969>.
- [27] R.D. Tang, D.X. Gong, Y.Y. Zhou, Y.C. Deng, C.Y. Feng, S. Xiong, Y. Huang, G. W. Peng, L. Li, Z.P. Zhou, Unique g-C₃N₄/PDI-g-C₃N₄ homojunction with synergistic piezo-photocatalytic effect for aquatic contaminant control and H₂O₂ generation under visible light, *Appl. Catal. B Environ.* 303 (2022), 120929, <https://doi.org/10.1016/j.apcatb.2021.120929>.
- [28] M.B. Duan, L.B. Jiang, B.B. Shao, C.Y. Feng, H.B. Yu, H. Guo, H.Y. Chen, W. W. Tang, Enhanced visible-light photocatalytic degradation activity of Ti₃C₂/PDIsM via π-π interaction and interfacial charge separation: experimental and theoretical investigations, *Appl. Catal. B Environ.* 297 (2021), 120439, <https://doi.org/10.1016/j.apcatb.2021.120439>.
- [29] Y. Yu, W. Yan, X. Wang, P. Li, W. Gao, H. Zou, S. Wu, K. Ding, Surface engineering for extremely enhanced charge separation and photocatalytic hydrogen evolution on g-C₃N₄, *Adv. Mater.* 30 (2018), 1705060, <https://doi.org/10.1002/adma.201705060>.
- [30] S. Zhang, J. Shi, Y. Sun, Y. Wu, Y. Zhang, Z. Cai, Y. Chen, C. You, P. Han, Z. Jiang, Artificial thylakoid for the coordinated photoenzymatic reduction of carbon dioxide, *ACS Catal.* 9 (2019) 3913–3925, <https://doi.org/10.1021/acscatal.9b00255>.
- [31] J.Y. Wang, Y. Cui, D. Wang, Design of hollow nanostructures for energy storage, conversion and production, *Adv. Mater.* 31 (2019), 1801993, <https://doi.org/10.1002/adma.201801993>.
- [32] W. Wang, J.J. Fang, S.F. Shao, M. Lai, C.H. Lu, Compact and uniform TiO₂@g-C₃N₄ core-shell quantum heterojunction for photocatalytic degradation of tetracycline antibiotics, *Appl. Catal. B Environ.* 217 (2017) 57–64, <https://doi.org/10.1016/j.apcatb.2017.05.037>.
- [33] M.G. Liu, H. Xia, W.X. Yang, X.Y. Liu, J. Xiang, X.M. Wang, L.S. Hu, F.S. Lu, Novel Cu-Fe bi-metal oxide quantum dots coupled g-C₃N₄ nanosheets with H₂O₂ adsorption-activation trade-off for efficient photo-fenton catalysis, *Appl. Catal. B Environ.* 301 (2022), 120765, <https://doi.org/10.1016/j.apcatb.2021.120765>.
- [34] X.X. Peng, J.W. Li, L.C. Yi, X. Liu, J.X. Chen, P.W. Cai, Z.H. Wen, Ultrathin ZnIn₂S₄ nanosheets decorating PPY nanotubes toward simultaneous photocatalytic H₂ production and 1,4-benzenedimethanol valorization, *Appl. Catal. B Environ.* 300 (2022), 120737, <https://doi.org/10.1016/j.apcatb.2021.120737>.
- [35] D.D. Gao, J.C. Xu, L.X. Wang, B.C. Zhu, H.G. Yu, J.G. Yu, Optimizing atomic hydrogen desorption of sulfur-rich NiS_{1+x} cocatalyst for boosting photocatalytic H₂ evolution, *Adv. Mater.* (2021), 2108475, <https://doi.org/10.1002/adma.202108475>.
- [36] L. Jiao, Y. Wang, H.L. Jiang, Q. Xu, Metal-organic frameworks as platforms for catalytic applications, *Adv. Mater.* 30 (2018), 1703663, <https://doi.org/10.1002/adma.201703663>.
- [37] Q. Li, L.M. Zhang, J.N. Liu, J. Zhou, Y.Q. Jiao, X.D. Xiao, C. Zhao, Y. Zhou, S. Ye, B. J. Jiang, J. Liu, Porous carbon nitride thin strip: precise carbon doping regulating delocalized pi-electron induces elevated photocatalytic hydrogen evolution, *Small* 17 (2021), 2006622, <https://doi.org/10.1002/smll.202006622>.
- [38] G.Y. Zhai, Y.H. Liu, Y.Y. Mao, H.G. Zhang, L.T. Lin, Y.J. Li, Z.Y. Wang, H.F. Cheng, P. Wang, Z.K. Zheng, Y. Dai, B.B. Huang, Improved photocatalytic CO₂ and epoxides cycloaddition via the synergistic effect of lewis acidity and charge separation over Zn modified UiO-bpydc, *Appl. Catal. B Environ.* 301 (2022), 120793, <https://doi.org/10.1016/j.apcatb.2021.120793>.
- [39] H. Cheng, H.F. Lv, J. Cheng, L. Wang, X.J. Wu, H.X. Xu, Rational design of covalent heptazine frameworks with spatially separated redox centers for high-efficiency photocatalytic hydrogen peroxide production, *Adv. Mater.* (2021), 2107480, <https://doi.org/10.1002/adma.202107480>.
- [40] J. Ryu, S.H. Lee, D.H. Nam, C.B. Park, Rational design and engineering of quantum-dot-sensitized TiO₂ nanotube arrays for artificial photosynthesis, *Adv. Mater.* 23 (2011) 1883–1888, <https://doi.org/10.1002/adma.201004576>.
- [41] J. Kim, S.H. Lee, F. Tieves, D.S. Choi, F. Hollmann, C.E. Paul, C.B. Park, Biocatalytic C=C bond reduction through carbon nanodot-sensitized regeneration of NADH analogues, *Angew. Chem. Int. Ed.* 57 (2018) 13825–13828, <https://doi.org/10.1002/anie.201804409>.
- [42] K.T. Oppelt, J. Gasiorowski, D.A.M. Egbe, J.P. Kollender, M. Himmelsbach, A. W. Hassel, N.S. Sariciftci, G. Knörl, Rhodium-coordinated poly(arylene-ethynylene)-alt-poly(arylenevinylene) copolymer acting as photocatalyst for visible-light-powered NAD⁺/NADH reduction, *J. Am. Chem. Soc.* 136 (2014) 12721–12729, <https://doi.org/10.1021/ja506060u>.
- [43] Z. Tong, D. Yang, Z. Li, Y. Nan, F. Ding, Y. Shen, Z. Jiang, Thylakoid-inspired multishell g-C₃N₄ nanocapsules with enhanced visible-light harvesting and electron transfer properties for high-efficiency photocatalysis, *ACS Nano* 11 (2017) 1103–1112, <https://doi.org/10.1021/acsnano.6b08251>.
- [44] J.F. Moulder, W.F. Stickle, P.E. Sobol, K.D. Bomben, *Handbook of X-ray Photoelectron Spectroscopy*, third ed., Physical Electronics, Inc., Minnesota, 1995.
- [45] H.H. Tran, P.H. Nguyen, V.H. Cao, L.T. Nguyen, V.M. Tran, M.L.P. Le, S.J. Kim, V. Vo, SnO₂ nanosheets/graphite oxide/g-C₃N₄ composite as enhanced performance anode material for lithium ion batteries, *Chem. Phys. Lett.* 715 (2019) 284–292, <https://doi.org/10.1016/j.cplett.2018.11.052>.
- [46] M. Kasinathan, S. Thiripurathanagan, A. Sivakumar, A facile fabrication of Br-modified g-C₃N₄/rGO composite catalyst for enhanced visible photocatalytic activity toward the degradation of harmful dyes, *Mater. Res. Bull.* 29 (2017) 8299–8312, <https://doi.org/10.1016/j.materresbull.2020.110870>.
- [47] B. Jurgens, E. Irran, J. Senker, P. Kroll, H. Muller, W. Schnick, Melem (2,5,8-triamino-tri-s-triazine), an important intermediate during condensation of melamine rings to graphitic carbon nitride: synthesis, structure determination by X-ray powder diffractometry, solid-state NMR, and theoretical studies, *J. Am. Chem. Soc.* 125 (2003) 10288–10300, <https://doi.org/10.1021/ja0357689>.
- [48] Y.J. Cui, Z.X. Ding, X.Z. Fu, X.C. Wang, Construction of conjugated carbon nitride nanoarchitectures in solution at low temperatures for photoredox catalysis, *Angew. Chem. Int. Ed.* 51 (2012) 11814–11818, <https://doi.org/10.1002/anie.201206534>.
- [49] V.W.H. Lau, I. Moudrakovski, T. Botari, S. Weinberger, M.B. Mesch, V. Duppel, J. Senker, V. Blum, B.V. Lotsch, Rational design of carbon nitride photocatalysts by identification of cyanamide defects as catalytically relevant sites, *Nat. Commun.* 7 (2016) 12165, <https://doi.org/10.1038/ncomms12165>.
- [50] X. Lu, G. Hou, *NMR spectroscopy*, in: Z. Wang, U. Wille, E. Juaristi (Eds.), *Encyclopedia of Physical Organic Chemistry*, John Wiley & Sons Inc, Hoboken, 2017, pp. 2819–2860.
- [51] G.W. Kim, Y.H. Son, H.I. Yang, J.H. Park, I.J. Ko, R. Lampande, J. Sakong, M. J. Maeng, J.A. Hong, J.Y. Lee, Y. Park, J.H. Kwon, Diphenanthroline electron transport materials for the efficient charge generation unit in tandem organic light-emitting diodes, *Chem. Mater.* 29 (2017) 8299–8312, <https://doi.org/10.1021/acs.chemmater.7b02655>.
- [52] X.C. Wang, K. Maeda, A. Thomas, K. Takanabe, G. Xin, J.M. Carlsson, K. Domen, M. Antonietti, A metal-free polymeric photocatalyst for hydrogen production from

- water under visible light, *Nat. Mater.* 8 (2009) 76–80, <https://doi.org/10.1038/NMAT2317>.
- [53] M. Tabbal, T. Christidis, S. Isber, P. Merel, M.A. El Khakani, M. Chaker, A. Amassian, L. Martinu, Correlation between the sp^2 -phase nanostructure and the physical properties of unhydrogenated carbon nitride, *J. Appl. Phys.* 98 (2005), 044310, <https://doi.org/10.1063/1.2009817>.
- [54] J.S. Zhang, G.G. Zhang, X.F. Chen, S. Lin, L. Mohlmann, G. Dolega, G. Lipner, M. Antonietti, S. Blechert, X.C. Wang, Co-monomer control of carbon nitride semiconductors to optimize hydrogen evolution with visible light, *Angew. Chem. Int. Ed.* 51 (2012) 3183–3187, <https://doi.org/10.1002/anie.201106656>.
- [55] A.E. Giannakas, E. Seristatidou, Y. Deligiannakis, I. Konstantinou, Photocatalytic activity of N-doped and N-F co-doped TiO_2 and reduction of chromium (VI) in aqueous solution: an EPR study, *Appl. Catal. B Environ.* 132 (2013) 460–468, <https://doi.org/10.1016/j.apcatb.2012.12.017>.
- [56] O. Al-Madanat, B.N. Nunes, Y. AlSalka, A. Hakki, M. Curti, A.O.T. Patrocínio, D. W. Bahnenmann, Application of EPR spectroscopy in TiO_2 and Nb_2O_5 photocatalysis, *Catalysts* 11 (2021) 1514, <https://doi.org/10.3390/catal11121514>.
- [57] Z.F. Hu, L.Y. Yuan, Z.F. Liu, Z.R. Shen, J.C. Yu, An elemental phosphorus photocatalyst with a record high hydrogen evolution efficiency, *Angew. Chem. Int. Ed.* 55 (2016) 9580–9585, <https://doi.org/10.1002/anie.201603331>.
- [58] D.W. Wakerley, M.F. Kuehnle, K.L. Orchard, K.H. Ly, T.E. Rosser, E. Reisner, Solar-driven reforming of lignocellulose to H_2 with a $CdS/CdOx$ photocatalyst, *Nat. Energy* 2 (2017) 17021, <https://doi.org/10.1038/nenergy.2017.21>.
- [59] L. Francàs, R. Matheu, E. Pastor, A. Reynal, S. Berardi, X. Sala, A. Llobet, J. R. Durrant, Kinetic analysis of an efficient molecular light-driven water oxidation system, *ACS Catal.* 7 (2017) 5142–5150, <https://doi.org/10.1021/acscatal.7b01357>.